

# A Measurement of Solar $pp$ Neutrino Flux using PandaX-4T Electron Recoil Data

Xiaoying Lu,<sup>2,3</sup> Abdusalam Abdukerim,<sup>4</sup> Zihao Bo,<sup>4</sup> Wei Chen,<sup>4</sup> Xun Chen,<sup>4,5</sup> Chen Cheng,<sup>6</sup> Zhaokan Cheng,<sup>7</sup> Xiangyi Cui,<sup>1</sup> Yingjie Fan,<sup>8</sup> Deqing Fang,<sup>9</sup> Changbo Fu,<sup>9</sup> Mengting Fu,<sup>10</sup> Lisheng Geng,<sup>11,12,13</sup> Karl Giboni,<sup>4</sup> Linhui Gu,<sup>4</sup> Xuyuan Guo,<sup>14</sup> Chencheng Han,<sup>1</sup> Ke Han,<sup>4,\*</sup> Changda He,<sup>4</sup> Jinrong He,<sup>14</sup> Di Huang,<sup>4</sup> Yanlin Huang,<sup>15</sup> Junting Huang,<sup>4</sup> Zhou Huang,<sup>4</sup> Ruquan Hou,<sup>5</sup> Yu Hou,<sup>16</sup> Xiangdong Ji,<sup>17</sup> Yonglin Ju,<sup>16</sup> Chenxiang Li,<sup>4</sup> Jiafu Li,<sup>6</sup> Mingchuan Li,<sup>14</sup> Shuaijie Li,<sup>1</sup> Tao Li,<sup>7</sup> Qing Lin,<sup>18,19</sup> Jianglai Liu,<sup>1,4,5,†</sup> Congcong Lu,<sup>16</sup> Lingyin Luo,<sup>10</sup> Yunyang Luo,<sup>19</sup> Wenbo Ma,<sup>4</sup> Yugang Ma,<sup>9</sup> Yajun Mao,<sup>10</sup> Yue Meng,<sup>4,5</sup> Xuyang Ning,<sup>4</sup> Binyu Pang,<sup>2,3</sup> Ningchun Qi,<sup>14</sup> Zhicheng Qian,<sup>4</sup> Xiangxiang Ren,<sup>2,3</sup> Nasir Shaheed,<sup>2,3</sup> Xiaofeng Shang,<sup>4</sup> Xiyuan Shao,<sup>20</sup> Guofang Shen,<sup>11</sup> Lin Si,<sup>4</sup> Wenliang Sun,<sup>14</sup> Andi Tan,<sup>17</sup> Yi Tao,<sup>4,5</sup> Anqing Wang,<sup>2,3</sup> Meng Wang,<sup>2,3</sup> Qihong Wang,<sup>9</sup> Shaobo Wang,<sup>4,21</sup> Siguang Wang,<sup>10</sup> Wei Wang,<sup>7,6</sup> Xiuli Wang,<sup>16</sup> Zhou Wang,<sup>4,5,1</sup> Yuehuan Wei,<sup>7</sup> Mengmeng Wu,<sup>6</sup> Weihao Wu,<sup>4</sup> Jingkai Xia,<sup>4</sup> Mengjiao Xiao,<sup>4</sup> Xiang Xiao,<sup>6</sup> Pengwei Xie,<sup>1</sup> Binbin Yan,<sup>1,‡</sup> Xiyu Yan,<sup>22</sup> Jijun Yang,<sup>4</sup> Yong Yang,<sup>4</sup> Yukun Yao,<sup>4</sup> Chunxu Yu,<sup>20</sup> Ying Yuan,<sup>4</sup> Zhe Yuan,<sup>9</sup> Xinning Zeng,<sup>4</sup> Dan Zhang,<sup>17</sup> Minzhen Zhang,<sup>4</sup> Peng Zhang,<sup>14</sup> Shibo Zhang,<sup>4</sup> Shu Zhang,<sup>6</sup> Tao Zhang,<sup>4</sup> Wei Zhang,<sup>1</sup> Yang Zhang,<sup>2,3</sup> Yingxin Zhang,<sup>2,3</sup> Yuanyuan Zhang,<sup>1</sup> Li Zhao,<sup>4</sup> Qibin Zheng,<sup>15</sup> Jifang Zhou,<sup>14</sup> Ning Zhou,<sup>4,5</sup> Xiaopeng Zhou,<sup>11</sup> Yong Zhou,<sup>14</sup> and Yubo Zhou<sup>4</sup>

(PandaX Collaboration)

<sup>1</sup>*Tsung-Dao Lee Institute, Shanghai Jiao Tong University, Shanghai, 200240, China*

<sup>2</sup>*Research Center for Particle Science and Technology, Institute of Frontier and Interdisciplinary Science, Shandong University, Qingdao 266237, Shandong, China*

<sup>3</sup>*Key Laboratory of Particle Physics and Particle Irradiation of Ministry of Education, Shandong University, Qingdao 266237, Shandong, China*

<sup>4</sup>*School of Physics and Astronomy, Shanghai Jiao Tong University, Key Laboratory for Particle Astrophysics and Cosmology (MoE), Shanghai Key Laboratory for Particle Physics and Cosmology, Shanghai 200240, China*

<sup>5</sup>*Shanghai Jiao Tong University Sichuan Research Institute, Chengdu 610213, China*

<sup>6</sup>*School of Physics, Sun Yat-Sen University, Guangzhou 510275, China*

<sup>7</sup>*Sino-French Institute of Nuclear Engineering and Technology, Sun Yat-Sen University, Zhuhai, 519082, China*

<sup>8</sup>*Department of Physics, Yantai University, Yantai 264005, China*

<sup>9</sup>*Key Laboratory of Nuclear Physics and Ion-beam Application (MOE), Institute of Modern Physics, Fudan University, Shanghai 200433, China*

<sup>10</sup>*School of Physics, Peking University, Beijing 100871, China*

<sup>11</sup>*School of Physics, Beihang University, Beijing 102206, China*

<sup>12</sup>*International Research Center for Nuclei and Particles in the Cosmos & Beijing Key Laboratory of Advanced Nuclear Materials and Physics, Beihang University, Beijing 100191, China*

<sup>13</sup>*School of Physics and Microelectronics, Zhengzhou University, Zhengzhou, Henan 450001, China*

<sup>14</sup>*Yalong River Hydropower Development Company, Ltd., 288 Shuanglin Road, Chengdu 610051, China*

<sup>15</sup>*School of Medical Instrument and Food Engineering, University of Shanghai for Science and Technology, Shanghai 200093, China*

<sup>16</sup>*School of Mechanical Engineering, Shanghai Jiao Tong University, Shanghai 200240, China*

<sup>17</sup>*Department of Physics, University of Maryland, College Park, Maryland 20742, USA*

<sup>18</sup>*State Key Laboratory of Particle Detection and Electronics, University of Science and Technology of China, Hefei 230026, China*

<sup>19</sup>*Department of Modern Physics, University of Science and Technology of China, Hefei 230026, China*

<sup>20</sup>*School of Physics, Nankai University, Tianjin 300071, China*

<sup>21</sup>*SJTU Paris Elite Institute of Technology, Shanghai Jiao Tong University, Shanghai, 200240, China*

<sup>22</sup>*School of Physics and Astronomy, Sun Yat-Sen University, Zhuhai, 519082, China*

(Dated: January 17, 2024)

The proton-proton ( $pp$ ) fusion chain dominates the neutrino production from the Sun. The uncertainty of the predicted  $pp$  neutrino flux is at the sub-percent level, whereas that of the best measurement is  $\mathcal{O}(10\%)$ . Furthermore, no direct measurement has been made via electron scattering below 165 keV recoil energy. Using the PandaX-4T commissioning data with 0.63 tonne $\times$ year of exposure, we perform the first measurement of solar  $pp$  neutrinos in the recoil energy range from 24 to 144 keV. The  $pp$  neutrino flux is measured to be  $(10.3 \pm 3.7 \text{ (stat.)} \pm 9.6 \text{ (syst.)}) \times 10^{10} \text{ s}^{-1} \text{ cm}^{-2}$ , consistent with Standard Solar Model and existing measurements.

According to the Standard Solar Model (SSM) [1–3], approximately 99% of the solar power comes from a series of reactions fusing hydrogen into helium. Neutrinos emitted in the initial fusion of two protons to a deuteron

constitute roughly 91% of the total solar neutrino flux. These neutrinos are commonly referred to as the  $pp$  neutrinos. The sub-dominant neutrinos from electron capture of  $^7\text{Be}$  account for an additional 7% of the flux. The

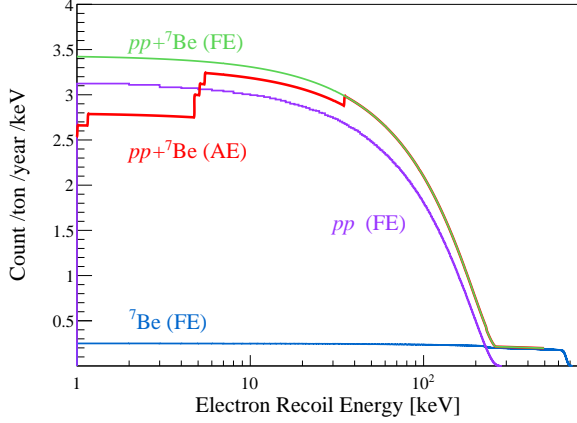


FIG. 1. Neutrino-electron elastic scattering spectrum of solar neutrinos with xenon electrons. If the binding energy of atomic electrons (AE) is considered (red curve), the scattering event rate in our ROI is lower than the free electron (FE) scenario (green curve). Adopted from Ref. [16].

weakly interacting neutrinos carry original information from solar fusion reactions. The precise measurement of solar neutrino flux is essential for verifying the SSM and shedding light on the solar metallicity puzzle [4]. Solar neutrinos are also crucial for neutrino physics, especially for understanding the matter effect of neutrino oscillation [5]. The solar luminosity has been measured to a 0.6% precision. In contrast, the  $pp$  neutrino flux has only been measured by Borexino with a precision of  $\mathcal{O}(10\%)$  with recoil energy threshold at 165 keV [6, 7].

A number of multi-tonne-scale liquid xenon (LXe) experiments including PandaX-4T [8], LZ [9] and XENONnT [10] are under operation to search for dark matter particles, coherent scattering of solar neutrinos on xenon nuclei [11, 12], and possible abnormal magnetic moments of neutrinos [13–15] in the few or few-tens of keV-scale electron or nuclear recoil energy. By design, these detectors also effectively cover over an electron recoil energy up to several hundred keV, spanning the majority of region of interest (ROI) for the  $pp$  neutrino flux.

The neutrino and electron interact via the electroweak force through the exchange of a Z or W boson, the latter of which is only possible for an electron neutrino. The solar  $pp$  neutrinos have a continuous energy spectrum with an endpoint at 420 keV. The  ${}^7\text{Be}$  neutrinos are monoenergetic at 384 keV (approximately 10%) and 862 keV (90%). The expected event rate per unit recoil energy is

$$\frac{dR}{dE_r} = N \sum_j \int \phi(E_\nu) P_{ej} \frac{d\sigma_j(E_\nu, E_r)}{dE_r} dE_\nu, \quad (1)$$

where  $N$  is the number of target electrons,  $\phi(E_\nu)$  is the neutrino flux as a function of neutrino energy,  $P_{ej}$  ( $j = e, \mu, \tau$ ) is the oscillation probabilities of  $\nu_e$  into the

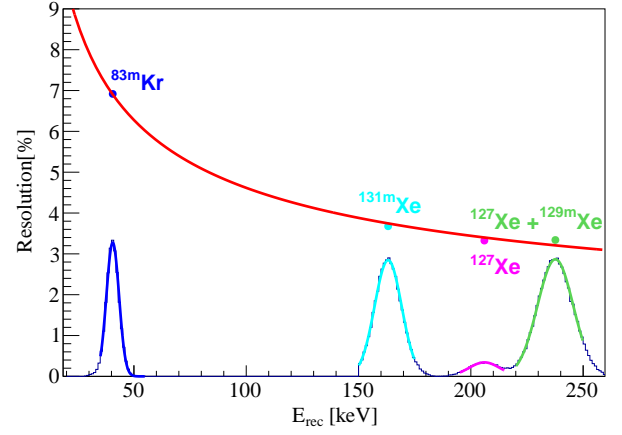


FIG. 2. The energy resolution using characteristic peaks at 41.6 keV, 163.9 keV, 208.1 keV, and 236.1 keV. The red curve shows the fit function  $\sigma/E = 0.40/\sqrt{E [\text{keV}]} + 0.0061$ .

flavor  $j$ , and  $d\sigma_j$  is the differential cross-section. Fig. 1 shows the energy spectrum of solar  $pp$  and  ${}^7\text{Be}$  neutrinos in a LXe detector, as given in Ref. [16]. When the xenon atomic effects are considered (adopted later in this paper), the rate in the ROI is suppressed by a few percent compared to the free electron scenario.

In this paper, we report the first measurement of the  $pp$  neutrino flux via their elastic scattering on electrons using the PandaX-4T detector located in the B2 hall of the China Jinping Underground Laboratory [17, 18]. The sensitive target of PandaX-4T has 3.69 tonne liquid xenon in a cylindrical dual-phase xenon time projection chamber (TPC) with 118.5 cm in diameter and 116.8 cm in height [19]. The prompt scintillation photons ( $S1$ ) and the delayed electroluminescence photons ( $S2$ ) are produced when a given energy is deposited in the sensitive volume. Both  $S1$  and  $S2$  signals are recorded by the top and bottom photomultipliers (PMT) arrays, which have 169 and 199 Hamamatsu 3-inch PMTs installed. Detailed discussions of the PandaX-4T detector can be found in Ref. [8].

This analysis selects different data from the existing analyses of the first commissioning data release [8, 11, 20]. The energy ROI is from 24 keV to 144 keV, with more than 60% of the solar  $pp$  neutrinos included. The lower boundary is chosen to be above the dark matter particle search region and the upper boundary to avoid the prominent 163.9 keV peak from  ${}^{131\text{m}}\text{Xe}$  produced in the neutron calibration runs. In the ROI, the detector noise has a negligible effect on both  $S1$  and  $S2$  signals. Therefore, we can recover approximately 9.5% exposure previously excluded in low energy analysis due to elevated detector noise. On the contrary, 8.4 days of data following a neutron calibration run is removed because of a high concentration of activated  ${}^{133}\text{Xe}$  and  ${}^{125}\text{I}$ . In the end, a total of 86.5 days is used for this analysis.

The PMT gains are calibrated with a newly implemented “rolling gain” approach for PMTs, which calculates PMT gains by fitting single photoelectron (SPE) spectra in individual PMTs run by run, adopted already in recent Ref. [19]. Our previous analyses calculated PMT gains with weekly light-emitting-diode (LED) calibration. To avoid biases in our data selections, cuts are first determined with LED-gain calibration data, validated with  $\sim 16\%$  of rolling gain physics data, and finally applied to the entire data set.

The quality cut variables are inherited from low energy analysis [8], but cut parameters are modified to suit the different energy windows. The main difference is the relaxation of the top and bottom PMT charge ratio requirement in the  $S2$  signal selection to accommodate the top  $S2$  saturation. The total quality cut efficiency is  $(99.1 \pm 0.1)\%$ . The solar  $pp$  neutrino signals scattering on electrons are primarily single-site (SS) events within the ROI. The identification of SS events follows the same procedure as in Ref. [8]. The SS efficiency is  $(99.7 \pm 0.1)\%$ , calculated using the  $^{220}\text{Rn}$  calibration data. A consistent efficiency is obtained using simulated data.

The horizontal position reconstruction follows the same procedure in Ref. [19], where de-saturated waveforms and improved optical Monte Carlo simulation are used. The reconstruction uniformity is confirmed with the diffusive  $^{83\text{m}}\text{Kr}$  calibration source injected into the TPC [21]. The mono-energetic peak of  $^{83\text{m}}\text{Kr}$  is also used to generate an energy response map, and the corresponding correction procedure follows Ref. [8].

The energy in LXe TPC is reconstructed as in Refs. [22, 23]. The energy spectrum is further corrected using a quadratic function between reconstructed energy and true energy of characteristic peaks at 41.6 keV ( $^{83\text{m}}\text{Kr}$ ), 163.9 keV ( $^{131\text{m}}\text{Xe}$ ), 208.1 keV ( $^{127}\text{Xe}$ ), and 236.1 keV ( $^{129\text{m}}\text{Xe}$  and  $^{127}\text{Xe}$ ). After the correction, the residual offset of energy peaks in the ROI is smaller than 1 keV, which is considered as the systematic uncertainty of the energy reconstruction. The relative  $1\sigma$  energy resolution at 24 keV (144 keV) is 8.8% (3.9%), as shown in Fig. 2.

The fiducial volume (FV) cuts and events in the ROI are shown in Fig. 3 as dashed lines and blue dots, respectively. The FV selection is the same as in the low energy analysis geometrically, and a total of  $2.66 \pm 0.02$  tonne of LXe in the center of the TPC is used. The slight difference with respect to Ref. [8] is from the event position reconstruction.

The background sources in the ROI include radon and krypton impurities in liquid xenon, detector materials, and radioactive xenon isotopes. The expected background sources are listed in Table I and described below.

Low energy background events from  $^{222}\text{Rn}$  chain are mainly the  $\beta$  decay of  $^{214}\text{Pb}$  to the ground state of  $^{214}\text{Bi}$  [19]. The event ratio, defined as the fraction of  $^{214}\text{Pb}$  events in the ROI per decay, is determined from a dedicated calibration run with  $3.5 \times 10^5$   $^{214}\text{Pb}$  events

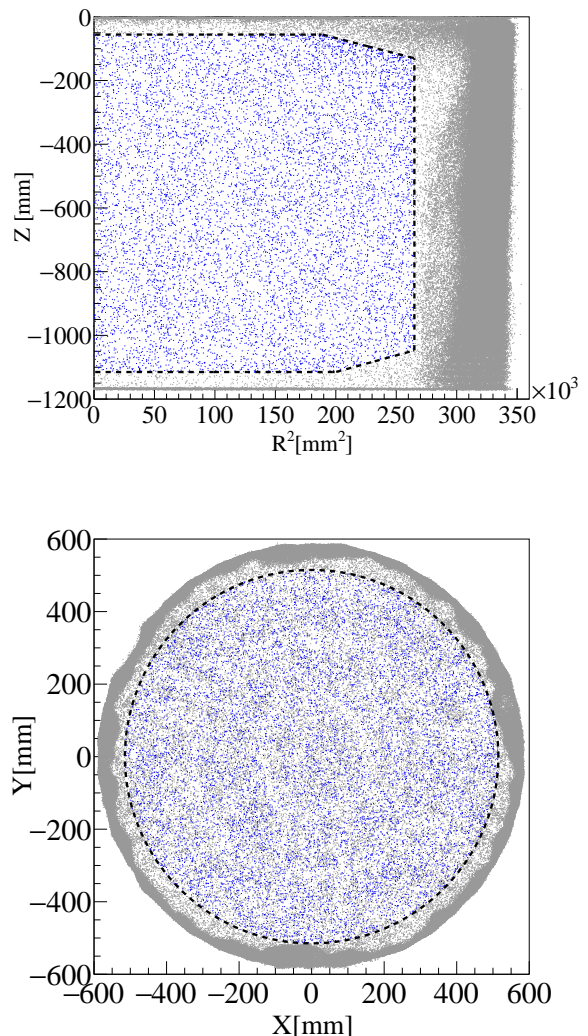


FIG. 3. The spatial distributions of the selected physics events in  $Z$  vs.  $R^2$  (top) and  $Y$  vs.  $X$  (bottom). The dashed lines show the boundary of the fiducial volume, and blue (gray) dots represent events inside (outside) the fiducial volume.

accumulated in about 11 days. The event ratio is measured to be  $0.039 \pm 0.001$ , with the uncertainty estimated based on the difference between our data and a recent theoretical prediction to accommodate the non-unique first-forbidden nature of the  $^{214}\text{Pb}$  decay [24]. The number of  $^{214}\text{Pb}$  events in the ROI is  $1865 \pm 110$ .

The  $\beta$  decay of  $^{214}\text{Bi}$  is a sub-dominate background component because it is rejected effectively by the  $^{214}\text{Bi}$ – $^{214}\text{Po}$  coincidence analysis. The  $^{214}\text{Bi}$ – $^{214}\text{Po}$  pairs are identified by an  $\alpha$  event following a  $\beta$  event in the subsequent 5 ms window. In the time window, the number of randomly paired events is negligible. We remove the identified  $^{214}\text{Bi}$ – $^{214}\text{Po}$  pairs from our spectrum, and the contribution from  $^{214}\text{Bi}$  is no longer included in the spectrum fit.

TABLE I. Expected and fitted background and signal counts in the ROI.

Components	Expected counts	Fitted counts
$^{214}\text{Pb}$	$1865 \pm 110$	$1845 \pm 113$
$^{212}\text{Pb}$	$276 \pm 71$	$270 \pm 80$
$^{85}\text{Kr}$	$489 \pm 254$	$405 \pm 249$
Material	$683 \pm 27$	$681 \pm 27$
$^{136}\text{Xe}$	$1009 \pm 46$	$999 \pm 47$
$^{133}\text{Xe}$	free	$4751 \pm 136$
Peak 1: [32-41] keV	free	$119 \pm 27$
Peak 2: [64-68] keV	free	$268 \pm 37$
$pp+^7\text{Be}$ neutrino	-	<b><math>297 \pm 260</math></b>

Similar to  $^{214}\text{Pb}$ , the expected contribution from  $\beta$  decay of  $^{212}\text{Pb}$  in  $^{220}\text{Rn}$  decay chain is determined from spectrum fit from higher energy analysis [19]. The maximum deviation of  $^{212}\text{Pb}/^{212}\text{Po}$  throughout the calibration period and stable decay period is considered as the systematic uncertainty. The expected number of events in the ROI is  $276 \pm 71$ . The concentration of  $^{85}\text{Kr}$  is  $0.52 \pm 0.27$  parts per trillion [19]. The expected contribution of  $^{85}\text{Kr}$  is  $489 \pm 254$  in the ROI. The levels of radioactivity from PMTs and detector vessels have been determined from the wide energy spectrum fit in Ref. [20]. The expected contribution in ROI is  $683 \pm 27$  events.

The expected background from  $^{136}\text{Xe}$   $2\nu\beta\beta$  is  $1009 \pm 46$  in the ROI, given by the half-life measured by PandaX-4T experiment with an exposure of  $15.5 \text{ kg}\times\text{year}$  of  $^{136}\text{Xe}$  isotope [20].

The contributions of  $^{133}\text{Xe}$ ,  $^{127}\text{Xe}$ ,  $^{125}\text{I}$ , and  $^{124}\text{Xe}$  are free and fitted in the final spectral analysis, as there are no constraints in our data outside the ROI.  $^{133}\text{Xe}$  from neutron activation during calibration contributes to the ROI with a distinctive rising slope starting at 81 keV in the energy spectrum. Cosmogenic  $^{127}\text{Xe}$ , introduced when some xenon exposed at the Earth's surface was filled into the detector during the data taking, contributes to the background with K-shell electron capture around 33.2 keV. Neutron-activated  $^{125}\text{Xe}$  decays quickly to the relatively long-lived  $^{125}\text{I}$  with a half-life of 59.4 days.  $^{125}\text{I}$  electron capture results in energy release of 67.3 keV (80% K-shell), 40.4 keV (16% L-shell), and 36.5 keV (3.5% M-shell) in the ROI. Thanks to the efficient removal capability of the xenon purification and circulation system, the effective lifetime of  $^{125}\text{I}$  in the TPC is significantly reduced and cannot be constrained by the isotopic lifetime. Two-neutrino double-electron capture of  $^{124}\text{Xe}$  (abundance  $\eta = 0.095\%$ ,  $Q = 2857 \text{ keV}$ ) deposits energy within our ROI at 64.3 keV and 32.3 - 37.3 keV [25, 26].

The spectrum fit is based on a binned likelihood procedure using the RooFit package [27]. Each background component is simulated using BambooMC [28], a Monte Carlo simulation package based on the Geant4 framework [29]. The contributions from  $^{214}\text{Pb}$ ,  $^{212}\text{Pb}$ ,  $^{85}\text{Kr}$ ,

TABLE II. Summary of contributions to systematic uncertainties. The contribution of each constrained parameter is extracted by turning on/off the corresponding penalty term in the fitter, assuming no correlation with other constraints. As a result, the quadrature combination of those rows is slightly different from the subtotal  $\sigma_{\text{constraint}}$  obtained directly by the fitter with all correlations properly built in.

	Components	Counts
$\sigma_{\text{constraint}}$	$^{85}\text{Kr}$	203
	$^{214}\text{Pb}$	87
	$^{212}\text{Pb}$	69
	Material	21
	$^{136}\text{Xe}$	19
	Peak 1 width	37
	Peak 2 width	33
	Data selection	30
	<b>Subtotal</b>	<b>237</b>
	Energy scale	111
$\sigma_{\text{manual}}$	Energy resolution	19
	Fit range	32
	$^{214}\text{Pb}$ spectrum	82
	$^{212}\text{Pb}$ spectrum	17
	$^{85}\text{Kr}$ spectrum	6
	<b>Subtotal</b>	<b>144</b>
	<b>Total</b>	<b>277</b>

detector material, and  $^{136}\text{Xe}$  are constrained using the uncertainties of the expected counts as described earlier and listed in Table I. Multiple mono-energetic peaks around 67 keV (33 keV) are grouped and modeled using a Gaussian function. The means of the Gaussian functions are free in the fit, while the sigmas are constrained by a fractional uncertainty of 20% of the measured resolutions in Fig. 2. The contributions of  $^{133}\text{Xe}$  and two Gaussian peaks are free-floating in the fit. The sum of solar  $pp$  and  $^7\text{Be}$  neutrino signals are combined into a single fit component.

The spectrum fit result is shown in Fig. 4. The number of solar  $pp+^7\text{Be}$  neutrino signals is  $297 \pm 260$ . Consistent results are obtained with a binned likelihood fit similar to that implemented in Ref. [20]. The fitted results of each background are listed in Table I. The background contributions from the material,  $^{85}\text{Kr}$ ,  $^{214}\text{Pb}$ , and  $^{212}\text{Pb}$  are consistent with the expected values. The fitted uncertainty includes a statistical ( $\sigma_{\text{stat.}}$ ) and a systematic ( $\sigma_{\text{constraint}}$ ) uncertainty of 107 and 237 events, respectively, extracted by comparing the signal uncertainties with and without the penalty terms for the systematic constraints. A similar *ad hoc* approach is used to extract the contribution from individual systematic effects later, assuming that extracted uncertainty is uncorrelated with the rest.  $^{133}\text{Xe}$  (free) is the largest background source, however its contribution to  $\sigma_{\text{stat.}}$  is relatively insignificant at 43 events due to its characteristic spectral shape.

Table II lists all the components of the systematic uncertainties. Among the constrained backgrounds,  $^{85}\text{Kr}$ ,  $^{214}\text{Pb}$  and  $^{212}\text{Pb}$  dominate the contribution to  $\sigma_{\text{constraint}}$  with an uncertainty of 203, 87, and 69 events, respec-

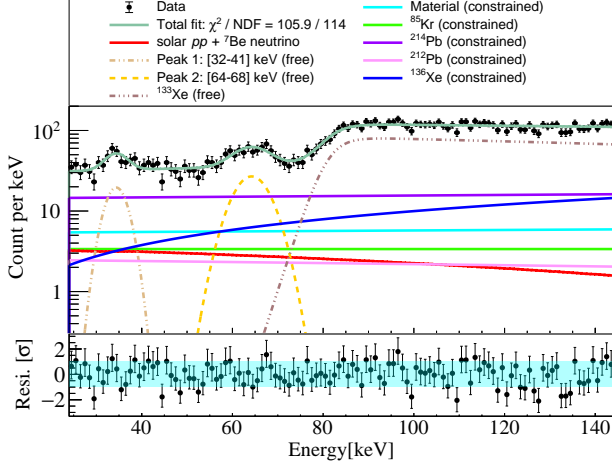


FIG. 4. (Color online) Result of the spectrum fit and the corresponding residual plot in the bottom panel. The solar  $pp+{}^7\text{Be}$  neutrino is shown as the red line. The constrained and free-floating backgrounds are shown in solid and dashed lines, respectively. The  $\chi^2/\text{NDF}$  (number of degrees of freedom, defined as the number of bins minus the number of free fit parameters) is shown in the legend.

tively. The constraints of two Gaussian peak widths give an uncertainty of 37 and 33 events, respectively. The uncertainties of data selection, including FV, quality cuts, and SS fraction, affect the uncertainty of the signal number proportionally with 30 events.

Additional sources of systematic uncertainties are evaluated manually ( $\sigma_{\text{manual}}$ ). The uncertainty from the reconstructed energy scale is introduced by shifting the energy spectrum by  $\pm 1$  keV and comparing the new fit results with the baseline fit, with a result of 111 events. To evaluate the contribution due to the energy resolution uncertainty, we perform the fit using PDFs with different energy resolution values. A  $\pm 1\sigma$  difference in energy resolution, where  $\sigma$  is from the aforementioned resolution function, propagates into an uncertainty of 19 events. The fit range uncertainty is evaluated to be 32 events by varying the ROI to 25 – 143 keV and 23 – 145 keV. The uncertainty introduced by  ${}^{214}\text{Pb}$  spectrum shape is calculated by changing the theoretical spectrum in the baseline fit to the shape measured in calibration data, leading to a result of 82 events. Similarly, the spectral shape differences between Geant4 [28] and a recent theoretical calculation of  ${}^{212}\text{Pb}$  and  ${}^{85}\text{Kr}$  [24] are also considered, and the introduced systematic uncertainties are found to be 17 and 6 respectively. In total, we get an overall systematic uncertainty of 277 events with 144 from  $\sigma_{\text{manual}}$ .

The final number of  $pp+{}^7\text{Be}$  neutrinos is  $297 \pm 107$  (stat.)  $\pm 277$  (syst.) from our analysis. The corresponding solar  $pp$  neutrino flux is  $(10.3 \pm 3.7$  (stat.)  $\pm 9.6$  (syst.))  $\times 10^{10} \text{ s}^{-1} \text{ cm}^{-2}$ , taking into account of the

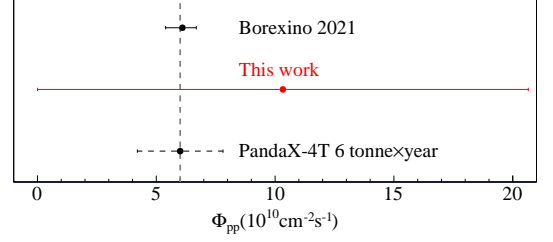


FIG. 5. The red dot and line show the result of solar  $pp$  neutrino flux, compared with the measurement from Borexino [7] and PandaX-4T projected measurement with 6 tonne $\times$ year exposure. The vertical dashed line is the average  $pp$  neutrino flux from the high-metallicity and low-metallicity SSM [4].

expected ratio of the  $pp$  and  ${}^7\text{Be}$  fluxes from SSM and their contributions in the ROI. The result is consistent with the SSM expectation [4] and the Borexino measurement [7], as shown in Fig. 5.

This analysis represents the first measurement for solar  $pp$  neutrino at low recoil energy and demonstrates the potential of multi-tonne-scale LXe detectors for solar neutrino studies in a completely new energy window. With an optimized online cryogenic distillation system, we expect to reduce the radon and krypton concentration by a factor of 1.8 or more [30]. Additional efforts, such as replacing TPC materials and circulation pumps, are being implemented for background control. Additional  ${}^{222}\text{Rn}$  calibration data and improved detector response with upgraded PMT readout circuit boards are expected to significantly reduce systematic uncertainties. Assuming radon and krypton levels of  $3.5 \mu\text{Bq/kg}$  and 0.25 ppt, respectively, negligible activation of xenon isotopes, and imposing a 5% constraint on all backgrounds, PandaX-4T can measure the solar  $pp$  neutrinos with an uncertainty of 30% with 6 tonne $\times$ year exposure.

This project is supported in part by the grants from National Science Foundation of China (Nos. 12090060, 12090063, 12105052, 12005131, 11905128, 11925502), and by the Office of Science and Technology, Shanghai Municipal Government (grant No. 22JC1410100). We thank the support from the Double First Class Plan of Shanghai Jiao Tong University. We also thank the sponsorship from the Chinese Academy of Sciences Center for Excellence in Particle Physics (CCEPP), Hongwen Foundation in Hong Kong, Tencent, and New Cornerstone Science Foundation in China. Finally, we thank the CJPL administration and the Yalong River Hydropower Development Company Ltd. for indispensable logistical support and other help.

\* Corresponding author: [ke.han@sjtu.edu.cn](mailto:ke.han@sjtu.edu.cn)

† Spokesperson: [jianglai.liu@sjtu.edu.cn](mailto:jianglai.liu@sjtu.edu.cn)

<sup>†</sup> Corresponding author: [yanbinbin@sjtu.edu.cn](mailto:yanbinbin@sjtu.edu.cn)

- [1] E. G. Adelberger et al., Solar fusion cross-sections, *Rev. Mod. Phys.* **70**, 1265 (1998), [arXiv:astro-ph/9805121](#).
- [2] S. Turck-Chieze et al., Solar neutrino emission deduced from a seismic model, *Astrophys. J. Lett.* **555**, L69 (2001).
- [3] E. G. Adelberger et al., Solar fusion cross sections II: the pp chain and CNO cycles, *Rev. Mod. Phys.* **83**, 195 (2011), [arXiv:1004.2318 \[nucl-ex\]](#).
- [4] N. Vinyoles, A. M. Serenelli, F. L. Villante, S. Basu, J. Bergström, M. C. Gonzalez-Garcia, M. Maltoni, C. Peña Garay, and N. Song, A new Generation of Standard Solar Models, *Astrophys. J.* **835**, 202 (2017), [arXiv:1611.09867 \[astro-ph.SR\]](#).
- [5] P. C. de Holanda and A. Y. Smirnov, LMA MSW solution of the solar neutrino problem and first KamLAND results, *JCAP* **02**, 001, [arXiv:hep-ph/0212270](#).
- [6] G. Bellini et al. (BOREXINO), Neutrinos from the primary proton–proton fusion process in the Sun, *Nature* **512**, 383 (2014).
- [7] S. Kumaran, L. Ludhova, O. Penek, and G. Settanta, Borexino Results on Neutrinos from the Sun and Earth, *Universe* **7**, 231 (2021), [arXiv:2105.13858 \[hep-ex\]](#).
- [8] Y. Meng et al. (PandaX-4T), Dark Matter Search Results from the PandaX-4T Commissioning Run, *Phys. Rev. Lett.* **127**, 261802 (2021), [arXiv:2107.13438 \[hep-ex\]](#).
- [9] D. S. Akerib et al. (LZ), Projected WIMP sensitivity of the LUX-ZEPLIN dark matter experiment, *Phys. Rev. D* **101**, 052002 (2020), [arXiv:1802.06039 \[astro-ph.IM\]](#).
- [10] E. Aprile et al. (XENON), Projected WIMP sensitivity of the XENONnT dark matter experiment, *JCAP* **11**, 031, [arXiv:2007.08796 \[physics.ins-det\]](#).
- [11] W. Ma et al. (PandaX), Search for Solar B8 Neutrinos in the PandaX-4T Experiment Using Neutrino-Nucleus Coherent Scattering, *Phys. Rev. Lett.* **130**, 021802 (2023), [arXiv:2207.04883 \[hep-ex\]](#).
- [12] E. Aprile et al. (XENON), Search for Coherent Elastic Scattering of Solar  $^8\text{B}$  Neutrinos in the XENON1T Dark Matter Experiment, *Phys. Rev. Lett.* **126**, 091301 (2021), [arXiv:2012.02846 \[hep-ex\]](#).
- [13] X. Zhou et al. (PandaX-II), A Search for Solar Axions and Anomalous Neutrino Magnetic Moment with the Complete PandaX-II Data, *Chin. Phys. Lett.* **38**, 011301 (2021), [Erratum: *Chin. Phys. Lett.* **38**, 109902 (2021)], [arXiv:2008.06485 \[hep-ex\]](#).
- [14] E. Aprile et al. (XENON), Excess electronic recoil events in XENON1T, *Phys. Rev. D* **102**, 072004 (2020), [arXiv:2006.09721 \[hep-ex\]](#).
- [15] J. Billard, L. Strigari, and E. Figueroa-Feliciano, Implication of neutrino backgrounds on the reach of next generation dark matter direct detection experiments, *Phys. Rev. D* **89**, 023524 (2014), [arXiv:1307.5458 \[hep-ph\]](#).
- [16] J.-W. Chen, H.-C. Chi, C. P. Liu, and C.-P. Wu, Low-energy electronic recoil in xenon detectors by solar neutrinos, *Phys. Lett. B* **774**, 656 (2017), [arXiv:1610.04177 \[hep-ex\]](#).
- [17] H. Ma et al. (CDEX), CDEX Dark Matter Experiment: Status and Prospects, *J. Phys. Conf. Ser.* **1342**, 012067 (2020), [arXiv:1712.06046 \[hep-ex\]](#).
- [18] J. Li, X. Ji, W. Haxton, and J. S. Y. Wang, The second-phase development of the China JinPing underground Laboratory, *Phys. Procedia* **61**, 576 (2015), [arXiv:1404.2651 \[physics.ins-det\]](#).
- [19] X. Yan et al. (PandaX), Searching for Two-Neutrino and Neutrinoless Double Beta Decay of  $^{134}\text{Xe}$  with the PandaX-4T Experiment (2023), [arXiv:2312.15632 \[nucl-ex\]](#).
- [20] L. Si et al. (PandaX), Determination of Double Beta Decay Half-Life of  $^{136}\text{Xe}$  with the PandaX-4T Natural Xenon Detector, *Research* **2022**, 9798721 (2022), [arXiv:2205.12809 \[nucl-ex\]](#).
- [21] D. Zhang et al., Rb83/Kr83m production and cross-section measurement with 3.4 MeV and 20 MeV proton beams, *Phys. Rev. C* **105**, 014604 (2022), [arXiv:2102.02490 \[nucl-ex\]](#).
- [22] M. Szydagis, N. Barry, K. Kazkaz, J. Mock, D. Stolp, M. Sweany, M. Tripathi, S. Uvarov, N. Walsh, and M. Woods, NEST: A Comprehensive Model for Scintillation Yield in Liquid Xenon, *JINST* **6**, P10002, [arXiv:1106.1613 \[physics.ins-det\]](#).
- [23] E. Aprile et al. (XENON), Energy resolution and linearity of XENON1T in the MeV energy range, *Eur. Phys. J. C* **80**, 785 (2020), [arXiv:2003.03825 \[physics.ins-det\]](#).
- [24] S. J. Haselschwardt, J. Kostensalo, X. Mougeot, and J. Suhonen, Improved calculations of beta decay backgrounds to new physics in liquid xenon detectors, *Phys. Rev. C* **102**, 065501 (2020), [arXiv:2007.13686 \[hep-ex\]](#).
- [25] E. Aprile et al. (XENON), Observation of two-neutrino double electron capture in  $^{124}\text{Xe}$  with XENON1T, *Nature* **568**, 532 (2019), [arXiv:1904.11002 \[nucl-ex\]](#).
- [26] E. Aprile et al. (XENON), Double-Weak Decays of  $^{124}\text{Xe}$  and  $^{136}\text{Xe}$  in the XENON1T and XENONnT Experiments, *Phys. Rev. C* **106**, 024328 (2022), [arXiv:2205.04158 \[hep-ex\]](#).
- [27] W. Verkerke and D. P. Kirkby, The RooFit toolkit for data modeling, eConf **C0303241**, MOLT007 (2003), [arXiv:physics/0306116](#).
- [28] X. Chen et al., BambooMC — A Geant4-based simulation program for the PandaX experiments, *JINST* **16** (09), T09004, [arXiv:2107.05935 \[physics.ins-det\]](#).
- [29] S. Agostinelli et al. (GEANT4), GEANT4—a simulation toolkit, *Nucl. Instrum. Meth. A* **506**, 250 (2003).
- [30] X. Cui et al., Design and commissioning of the PandaX-4T cryogenic distillation system for krypton and radon removal, *JINST* **16** (07), P07046, [arXiv:2012.02436 \[physics.ins-det\]](#).